JOURNAL OF SYNCHROTRON RADIATION
ISSN 1600-5775

Temperature-gradient analyzers for non-resonant inelastic X-ray scattering

Daisuke Ishikawa[a,b]* and Alfred Q. R. Baron[a,b]

[a]Materials Dynamics Laboratory, RIKEN SPring-8 Center, 1-1-1 Kouto, Sayo-cho, Sayo-gun, Hyogo 679-5198, Japan, and [b]Precision Spectroscopy Division, Center for Synchrotron Radiation Research, Japan Synchrotron Radiation Research Institute (JASRI), 1-1-1 Kouto, Sayo-cho, Sayo-gun, Hyogo 679-5148, Japan.
*Correspondence e-mail: disikawa@spring8.or.jp

Received 23 October 2020
Accepted 14 February 2021

Edited by P. A. Pianetta, SLAC National Accelerator Laboratory, USA

Keywords: inelastic X-ray scattering; analyzers; X-ray optics; electronic excitation.

The detailed fabrication and performance of the temperature-gradient analyzers that were simulated by Ishikawa & Baron [(2010). *J. Synchrotron Rad.* **17**, 12–24] are described and extended to include both quadratic and 2D gradients. The application of a temperature gradient compensates for geometric contributions to the energy resolution while allowing collection of a large solid angle, ∼50 mrad × 50 mrad, of scattered radiation. In particular, when operating relatively close to backscattering, $\pi/2 - \theta_B$ = 1.58 mrad, the application of a gradient of 1.32 K per 80 mm improves the measured total resolution from 60 to 25 meV at the full width at half-maximum, while when operating further from backscattering, $\pi/2 - \theta_B$ = 6.56 mrad, improvement from 330 to 32 meV is observed using a combination of a gradient of 6.2 K per 80 mm and dispersion compensation with a position-sensitive detector. In both cases, the operating energy was 15.8 keV and the incident bandwidth was 22 meV. Notably, the use of a temperature gradient allows a relatively large clearance at the sample, permitting installation of more complicated sample environments.

1. Introduction

Non-resonant inelastic X-ray scattering (NRIXS) has become a powerful tool for studying momentum-resolved atomic and electronic dynamics (Schülke, 2007; Baron, 2016, 2020). The NRIXS cross section is simply proportional to electron number density, so that one can investigate charge dynamics in materials straightforwardly, without the complications that can occur from intermediate states in resonant scattering. High multipole transitions are also observable at high-momentum transfers (Larson *et al.*, 2007; Haverkort *et al.*, 2007), which are not accessible via optical spectroscopy. In addition, the penetrating power of hard X-rays enables bulk-sensitive measurements and penetration into complex sample environments, *e.g.* to investigate samples under extreme conditions.

Spectrometers may be separated by the energy scale of the excitations that one wants to investigate, as there is usually a trade-off between resolution and available photon flux. High resolution (∼meV) enables phonons to be probed while medium resolution (∼50 to ∼200 meV) allows access to valence-shell excitations and the multipole order of the electronic transitions. At lower resolution (∼eV) the high flux allows access to core levels, charge transfer and plasmon excitations, as well as band structure. Resolution in the 10 to 30 meV range is interesting to investigate the detailed structure of electronic excitations, including crystal-field transitions and more complex excitations such as orbitons. Is it also

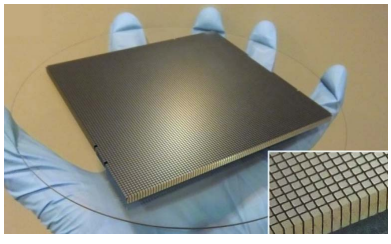

potentially useful for investigating weak/high-energy vibrational excitations (*e.g.* in hydrogen-containing materials).

Analyzers are the most critical and difficult component of IXS spectrometers and great effort has been invested in fabricating spherical crystal analyzers. For high (meV scale) resolution, diced spherical crystal analyzers have been utilized with higher-order Bragg back-reflections ($\theta_B \simeq \pi/2$) (Masciovecchio *et al.*, 1996; Baron *et al.*, 2000; Sinn, 2001; Sinn *et al.*, 2002; Verbeni *et al.*, 2005, 2009; Said *et al.*, 2011). These usually operate in a Rowland circle geometry (Burkel, 1991). One problem of using a Rowland geometry close to backscattering is that the sample space is limited so the detector must be moved away from the sample towards the analyzer crystals or Bragg angles must be chosen that are far from back-reflection. This results in a geometric contribution which degrades the energy resolution and has been called a 'demagnification contribution' (Burkel, 1991). The impact of this contribution tends to be worse when a two-dimension analyzer array is used, or when shorter sample–analyzer distances are used.

Temperature gradient (TG) analyzers have been considered in simulations (Ishikawa & Baron, 2010) as a way of reducing the demagnification contribution in a compact spectrometer. The TG analyzers reduce geometric aberration by gradually changing the d spacing over the analyzer. For high-resolution spectrometers, a TG has been shown to provide modest fractional improvements in resolution, *e.g.* from ∼0.9 to 0.75 meV (Ishikawa *et al.*, 2015). However, more dramatic improvements (factors of two or more) are expected in a medium-resolution setup. This performance was demonstrated by Ishikawa *et al.* (2017). Here, we investigate these analyzers in more detail. The present article discusses how to reduce the geometric aberration arising from an off-Rowland geometry while retaining large clearance (∼200 mm) between the detector and the sample. We measured the performance of analyzers installed in the 2 m medium-resolution IXS spectrometer at BL43LXU in SPring-8. The results are supported by detailed ray-tracing calculations.

This article is organized as follows. Section 2 reviews the basic concept of the TG analyzer. Section 3 describes the analyzer fabrication methods. Section 4 presents ray-tracing calculations and discusses TG contributions to the geometric aberrations. Section 5 explains details of TG control. The experimental results are discussed in Section 6 and our conclusions are given in Section 7.

2. Analyzer

We used diced analyzers operating within 7 mrad of backscattering. As the NRIXS cross section tends to be small compared with either phonon or resonant inelastic X-ray scattering (RIXS) cross sections, we accepted a large solid angle, ∼50 mrad × 50 mrad, to maximize count rates.

2.1. Analytic formulae for temperature-compensation correction

We briefly recall some basic concepts of the TG analyzer from the work of Ishikawa & Baron (2010). The total energy resolution of an IXS spectrometer ΔE_{tot} may be estimated as

$$\Delta E_{tot} = \left(\Delta E_{inc}^2 + \Delta E_{int}^2 + \Delta E_{geom}^2\right)^{1/2}, \quad (1)$$

where ΔE_{inc}, ΔE_{int} and ΔE_{geom} are the incident-energy resolution (bandwidth from the monochromator), the intrinsic analyzer reflection width and a geometric contribution, respectively. Here, we focus on ΔE_{geom}.

One contribution to the fractional energy resolution $\varepsilon \equiv (\Delta E/E)_{geom}$ of pixelated spherical analyzers operating on a Rowland geometry with a single-element detector (SED) is related to the analyzer crystallite size [see Fig. 1(*a*)], c, by

$$\varepsilon_1 = \left(\frac{c}{R}\right)\tan\delta_0, \quad (2)$$

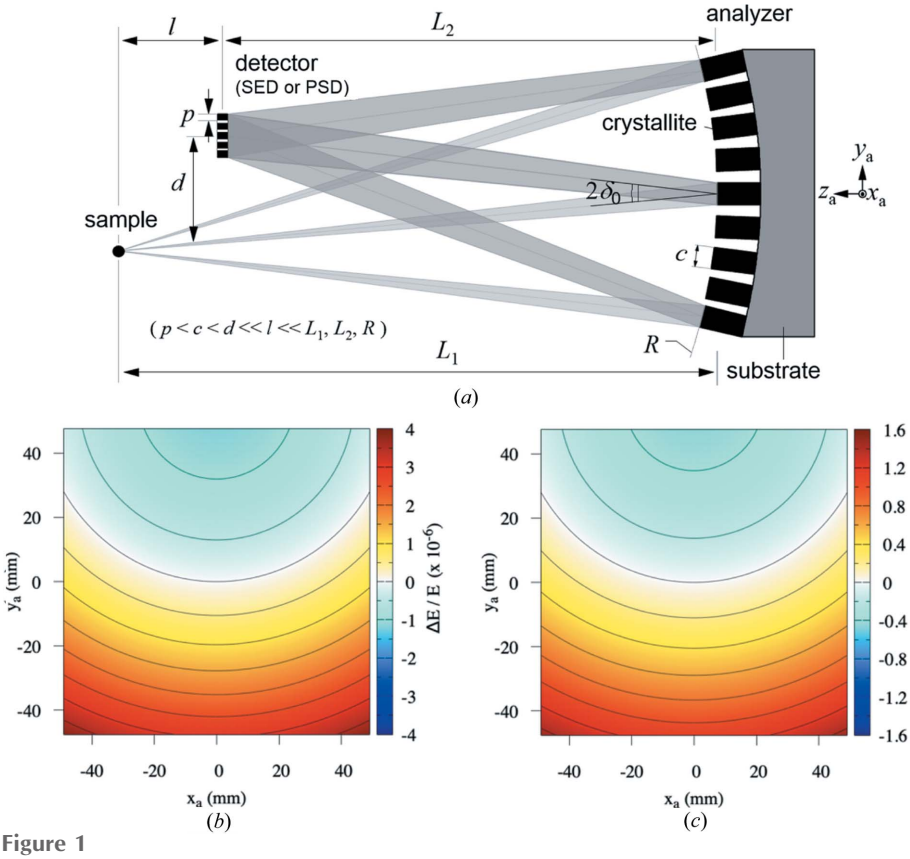

Figure 1
(*a*) A sketch of the IXS geometry. (*b*) Energy shift and (*c*) required temperature correction for the analyzer as a function of analyzer position for an Si analyzer near room temperature from equations (8) and (7). The geometry is off-Rowland with L_1 = 2005 mm, R = 1900 mm, M = 0.90 and d = 6 mm. The size of the analyzer pixels is neglected.

where E is the X-ray energy, R is the radius of curvature and δ_0 ($\equiv \pi/2 - \theta_B$) is the deviation angle from exact backscattering at the analyzer center. This can be improved by using a pixelated detector (Huotari *et al.*, 2006) with pixel size p, with

$$\varepsilon_2 = \frac{p}{2R}\tan\delta_0. \tag{3}$$

Assuming we desire $\varepsilon \simeq 1 \times 10^{-7}$ using a compact spectrometer ($R < \sim 2$ m) and $p = 0.1$ mm, then δ_0 must be <1 mrad [$d < 4$ mm, Fig. 1(*a*)]. This severely constrains sample environments. As a result, the pure Rowland geometry does not practically allow operation close to backscattering geometry in many cases. Therefore, the detector must be moved away from the sample, usually towards the analyzer crystal, so it is placed in front of the sample environments when viewed from the analyzer. This violates the Rowland circle condition and the resolution becomes worse owing to a demagnification contribution (Burkel, 1991; Ishikawa & Baron, 2010). This [see Fig. 1(*a*)] is estimated as

$$\varepsilon_3 = \Delta\delta\tan\delta_0 \cong \frac{\Omega d}{4R}\,\frac{1-M}{M}, \tag{4}$$

where $\Delta\delta$ is the magnitude of Bragg angle distribution over the analyzer, Ω is the solid angle of the analyzer in the analyzer scattering plane and M ($\equiv L_2/L_1$) is the magnification of the focusing geometry. Here, L_1 and L_2 are the sample–analyzer and analyzer–detector distance, respectively. L_1 and L_2 satisfy $1/L_1 + 1/L_2 = 1/(2R\cos\delta_0) \simeq 1/2R$.

A TG may be used to reduce the geometric contribution of equation (4). The TG creates a d-spacing variation of crystallites over the analyzer that compensates for the angle change of the beam reflected into the detector. The analytic formula for the required temperature correction, ΔT ($= T - T_0$), as a function of analyzer vertical direction (y_a) is given as (Ishikawa & Baron, 2010)

$$\Delta T(y_a) \cong \frac{1}{8\alpha(T_0)}\frac{1-M}{L_1M}\left(-4\delta_0 y_a + \frac{1-M}{L_1M}y_a^2\right), \tag{5}$$

where T_0 is the temperature at the center of the analyzer and $\alpha(T_0) \cong 2.63 \times 10^{-6}\ \mathrm{K}^{-1}$ is the thermal-expansion coefficient of Si at $T_0 = 300$ K calculated from references Okada & Tokumaru (1984), Watanabe *et al.* (2004) and Mohr *et al.* (2016). Note that the TG has a term linear in the vertical position, y_a, so must be inverted depending on the reflecting direction (upward or downward) of the analyzer as shown in Fig. 10.

2.2. Extension to 2D case

In addition to the quadratic term given in equation (5), there is another quadratic term related to the horizontal position on the analyzer, x_a, given by

$$\Delta T(x_a) \cong \frac{1}{8\alpha(T_0)}\left(\frac{1-M}{L_1M}\right)^2 x_a^2. \tag{6}$$

Hence, to second order, the ideal temperature correction as a function of analyzer position (x_a, y_a) can be written as

$$\Delta T(x_a, y_a) \cong Ay_a + By_a^2 + Cx_a^2, \tag{7}$$

where $A = -\delta_0\eta/[2\alpha(T_0)]$, $B = C = \eta^2/[8\alpha(T_0)]$, $\eta = (1 - M)/L_1M$ and T_0 is the temperature at the analyzer center ($x_a = y_a = 0$). The geometric contribution to the energy resolution is given by $\Delta E/E = \Delta d_h/d_h = \alpha(T)\Delta T$, where d_h is the d spacing of the diffraction plane. So one has

$$\frac{\Delta E(x_a, y_a)}{E} \cong A'y_a + B'y_a^2 + C'x_a^2, \tag{8}$$

where $A' = -\delta_0\eta/2$ and $B' = C' = \eta^2/8$. An example of the impact of these terms is shown in Fig. 1(*b*) for off-Rowland geometry with $L_1 = 2005$ mm, $M = 0.9$ and $d = 6$ mm. To correct the aberration, the temperature must be shifted as shown in Fig. 1(*c*). We consider four cases in detail: (*a*) uniform temperature (A, B, $C \neq 0$), (*b*) 1D linear TG ($A = 0$), (*c*) 1D quadratic TG ($A = B = 0$) and (*d*) 2D quadratic TG ($A = B = C = 0$).

Even with the proper TG applied, the resolution will still be limited by the pixel size if one uses an SED. An equation analogous to equation (1) above gives the best fractional energy resolution with an SED as

$$\varepsilon_1' = \frac{c}{L_1}\tan\delta_0. \tag{9}$$

By contrast, the fractional resolution with a position-sensitive detector (PSD) using dispersion compensation (DC) (Huotari *et al.*, 2006) is estimated to be (Ishikawa & Baron, 2010)

$$\varepsilon_4 \cong \frac{1}{8R}\left[\Omega\frac{1-M}{M}\left(\frac{c'}{2} - p\right) + \frac{4pd}{R}\right], \tag{10}$$

where $2c'$ [$\equiv c(1 + M)$] is the focal-spot size in the off-Rowland geometry.

Practically, while a fully 2D quadratic TG is the best temperature correction, it is difficult to achieve. Therefore, here we focus primarily on 1D corrections, both linear and quadratic.

2.3. Spectrometer parameters

The medium-resolution IXS spectrometer at BL43LXU was designed to give a total resolution of $\Delta E_{tot} \simeq 25$ meV with a short ($\sim$2 m) arm radius. The incident bandwidth from the medium-resolution monochromator is $\Delta E_{inc} = 22$ meV. To improve the tails of the resolution, the Si(888) back-reflection, $\Delta E_{int} = 4.4$ meV, was used for the analyzers. To obtain large space at the sample area, the analyzers were operated off the Rowland geometry with magnification $M \simeq 0.9$. The off-Rowland geometry is also advantageous for background reduction as the beam size remains small so the detector area can also be kept small, reducing the rate of background events from natural sources (cosmic rays). The radius of curvature of the spherical analyzer was selected to be $R = 1.9$ m.

To improve measurement efficiency, a 2D array of analyzers was used. This in turn forces larger deviations from exact backscattering and necessitates a large temperature correction. When the backscattering angle is $\delta_0 = 1$–10 mrad, the parameter A in equation (7) is estimated to be ~ -0.01 to

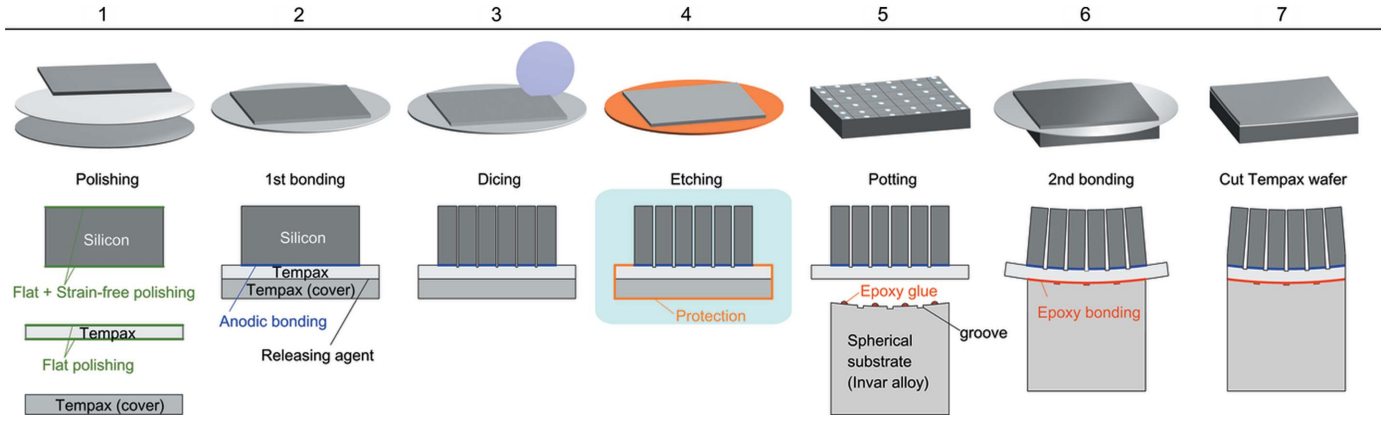

Figure 2
Schematics of the steps in analyzer fabrication. A two-step bonding process (first, anodic bonding; second, epoxy glue) was used. Details are given in the main text.

-0.1 K mm^{-1}. Therefore, $\Delta T \simeq$ 1–10 K is needed over an ~100 mm analyzer size. The required heat flow, Q, can be estimated by $Q = \lambda S \Delta T/h$. Here, λ is the thermal conductivity, S refers to the cross section, ΔT is the temperature offset and h refers to the distance to apply the TG. Then, a substrate material must be selected that has appropriate thermal conductivity, *i.e.* the conductivity of Si is too high and would require too high a power to generate the needed gradient. We selected Invar alloy, λ = 13 W m^{-1} K^{-1}, for the substrate. When applying $\Delta T \simeq$ 1–10 K over the analyzer using the Invar substrate (cross section S = 100 mm × 15 mm, height h = 95 mm), a 50 Ω resistance heater and a low-voltage power supply (5–23 V), one can control 0.5–10 W for creating the TG. If we had selected Si (148 W m^{-1} K^{-1}) as the substrate material, a factor of greater than ten larger heating and cooling capacity would be needed for creating the steady-state TG. On the other hand, choosing a glass (~1 W m^{-1} K^{-1}) would require a factor of ten smaller power, which might have a slow response and be difficult to stabilize.

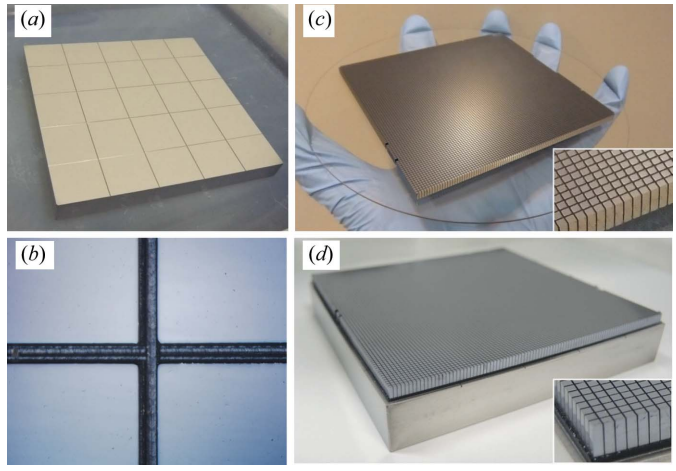

Figure 3
(*a*) Photograph of the spherical substrate made of Invar alloy with crossed grooves and (*b*) an enlarged view of the grooves. (*c*) Photograph after first bonding and dicing. (*d*) The completed analyzer.

3. Analyzer fabrication

Analyzer fabrication requires solving a number of technical problems while staying within the constraints needed for operation. In the present case, our constraints were (i) using a pixelated spherical analyzer on (ii) an Invar substrate with (iii) a small (~2 m) radius of curvature. In order to achieve good resolution, the Si also must be etched. To meet these conditions, we adopted a multi-step process with the following main steps (the details are given below). First, a flat Si wafer was attached to a glass wafer by anodic bonding. Then the Si wafer was diced and etched to eliminate residual strain. Finally, the bonded wafers were glued to a spherical substrate. It is important that these successive processing steps do not adversely affect the analyzer focusing properties, thus each step must not introduce large slope errors, <~10 µrad (r.m.s.) is highly desirable. The details of the fabrication process are as follows (see Fig. 2 for a schematic of each step and Fig. 3 for photographs at different stages in the fabrication process).

(1) Material preparation. An Si wafer (95 mm × 100 mm × t × 3.0 mm) was cut from high-purity single-crystal Si ingot (float zone, resistivity ≃ 4 kΩ cm). Then the surface of the wafer was polished strain free within a flatness of <2–3 fringes over the plane. In parallel, a TEMPAX Float (TPX) (Ø150 mm × t × 0.7 mm) wafer was polished with a flatness of <2–3 fringes (<1–1.5 λ). These wafers were ultrasonically cleaned with acetone and ethanol followed by a pure H_2O (<1 µS cm^{-1}) rinse. The wafers were dried using blown N_2 gas. UV/O_3 cleaning was then applied to eliminate inorganic residues followed by a rinse using pure H_2O and drying again using N_2 gas.

(2) Anodic bonding [see also Fig. 4(*a*)]. The assembly was performed using a desktop open clean bench (KOKEN LTD, KOACH) under ISO class 1 to eliminate dust. The anode electrode was a t = 20 µm SUS304 foil and the cathode electrode was a t = 0.2 mm graphite sheet. The t = 0.7 mm TPX wafer was attached to another TPX (t = 1 mm) cover to protect the 0.7 mm wafer from surface damage by Na and K

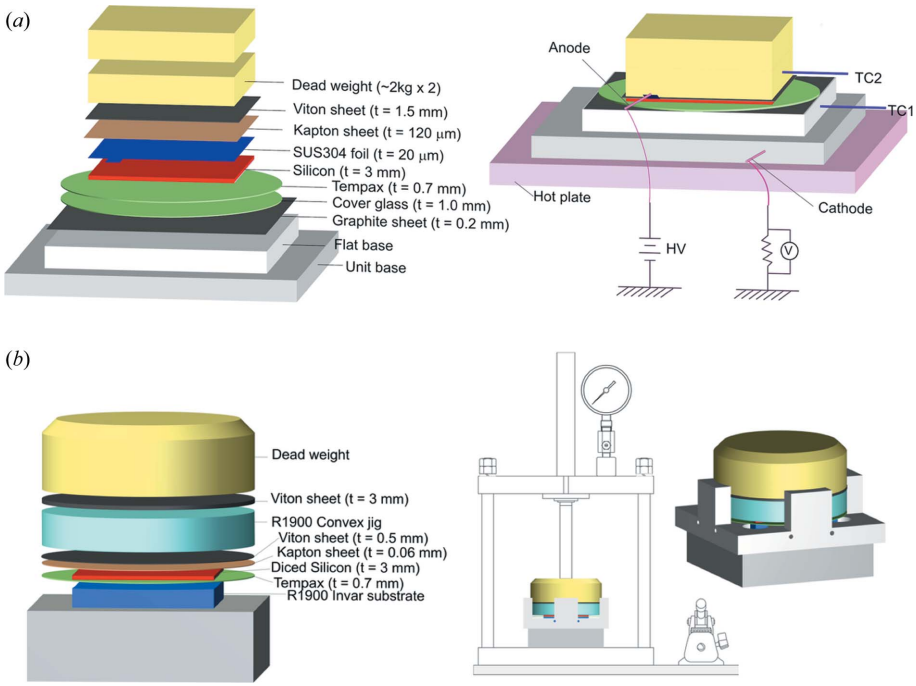

Figure 4
(*a*) A schematic of the first bonding between Si and TPX wafer using anodic bonding. (*b*) A schematic of the second bonding between Invar spherical substrate and Si/TPX wafer.

Table 1
Parameters for the pixelated spherical analyzer.

Substrate	Invar
Radius of curvature (mm)	$R = 1900 \pm 10$
Substrate size (mm)	$100 \times 95 \times 15$
Slope error (μrad)	<10 (r.m.s.)
Roughness (nm)	<2 (r.m.s.)
Active area (mm)	98×93
Si crystallite size (mm)	$0.87 \times 0.87 \times 3.0$
Pitch (mm)	1.0
Solid angle (mrad)	48.9×46.4 (maximum)

aggregations coming from inside the Tempax wafer. A small amount of silicone was used as releasing agent for the TPX wafers. Anodic bonding of Si/TPX wafer was performed at $T = 330$°C, $I_{max} = 3.0$ mA and $V = 0$–2.5 kV.

(3) Dicing. The Si/TPX wafer was diced on a 1.0 mm pitch with an 80 μm groove width. The groove depth was carefully controlled to be through the Si but only 0.03 mm into the TPX wafer.

(4) Etching. The diced Si was etched to remove the residual strain. A volume fraction of HF (46%) : HNO_3 (61%) : CH_3COOH (99.7%) = 3 : 5 : 3 was used as the etchant. The etching temperature and time were ~20°C and 90 s, respectively. The back of the TPX wafer was protected by attaching another piece of glass (see Fig. 2) that was then sealed on the edge by poly-tetra-fluoro-ethylene (PTFE) tape during the etching. This was sufficient to prevent damage to the bonded glass wafer. The final crystallite size was typically 0.87 mm × 0.87 mm × ~3 mm after etching. The cover glass was removed and then the Si/TPX wafer was cleaned as in (2).

(5) Invar substrate. The specification of the substrate is given in Table 1. The radius of curvature and slope error were $R = 1900$ mm and <10 μrad (r.m.s.), respectively. The spherical surface was cross grooved on a 15–20 mm pitch, 0.175 mm width and >0.6 mm depth [Figs. 3(*a*) and 3(*b*)] to provide an escape for the residual glue between the substrate and the Si/TPX wafer. Making a uniform epoxy glue bond was difficult and required several iterations to determine a successful protocol. For the first analyzers, no grooves were put in the substrate and the surface reflection profile had many voids from non-uniform gluing. Then we introduced grooves onto the substrate to eliminate residual glue. However, owing to the difficulty in machining Invar, it was difficult to make the grooves without disturbing the surface. We finally used spherical polishing after grooving to obtain a uniform response over the analyzer surface. Epoxy glue (EPO-TEK 301-2) was used for the second (spherical) bonding. A uniform amount of glue was potted on each grid on the substrate. This process was also performed using the clean bench mentioned in (2).

(6) Gluing. The setup for the gluing is shown in Fig. 4(*b*). A Kapton sheet ($t = 60$ μm) and a Viton sheet ($t = 0.5$ mm) were used for the interface materials. A standard convex jig ($R = 1900$ mm) and dead weight were inserted before applying external forces. A bench frame hydraulic press (ENERPAC CPF5-P142) was used to apply forces to the unit with a maximum of 0.7–1.0 kN. The force was applied for 5–7 days at room temperature until the glue cured. One should emphasize that this procedure required some fine tuning as, when we started, we used very low viscosity epoxy glue (EPO-TEK 301-2FL) with a large pressure (>1.5 kN) and essentially forced most of the glue into the grooves so the Si/TPX wafers sometimes 'popped up' from the spherical substrate after about 1 year.

(7) Trimming. The residual TPX was cut away from the rectangular substrate. The TPX was cut out 1 mm from the edge of the substrate, thus the final active area is 98 mm × 93 mm. Fig. 3(*d*) shows a completed analyzer.

4. Ray tracing

We carried out ray tracing in order to estimate analyzer performance and to confirm our understanding of our results. We used the three geometric conditions (d values) given in Table 2. The rays were assumed to uniformly irradiate the analyzer surface. We took the analyzer slope error to be 20 μrad × 20 μrad (r.m.s.) with a source size at the sample

Table 2
Geometric contributions to the energy resolution for uniform-temperature analyzers for the analyzer rows shown in Fig. 10.

Most of the parameters are defined in the main text. $\Delta\delta_{x,y}$ refers to the maximum deviation of Bragg angles owing to the demagnification contribution. In all cases, geometric energy resolution is the main contribution to the total resolution. L_1 and L_2 are determined by $1/L_1 + 1/L_2 = 1/(2R\cos\delta_0) \simeq 1/2R$.

Analyzer row	d (mm)	L_1 (mm)	L_2 (mm)	l (mm)	M	δ_0 (mrad)	$\Delta\delta_x$ (mrad)	$\Delta\delta_y$ (mrad)	ΔE_{geom} (meV)	ΔE_{int} (meV)	ΔE_{inc} (meV)	ΔE_{tot} (meV)
First	6	2005	1805	200	0.90	1.575	0.78	2.84	44	4.4	22	60
Third	10	2019	1794	225	0.89	2.622	0.77	2.84	101	4.4	22	100
Second	25	2019	1794	225	0.89	6.556	0.77	2.85	288	4.4	22	330

Table 3
Conditions for the ray-tracing calculations and calculated contributions to the energy resolution.

A, B, C: the parameters in equation (7). ΔE_{geom}^{SED}: the geometric energy resolution (FWHM) of the SED (2 mm × 2 mm for d = 6 mm, and ∼1.9 mm × 1.9 mm for d = 10 and 25 mm). ΔE_{geom}^{DC}: the geometric energy resolution (FWHM) using DC with a PSD [∼1.9 mm × 0.172 mm (11 × 1 pixels)]. The solid angles cover full analyzer acceptance (49 mrad × 46 mrad).

								Calculations (geometric)		
d (mm)	L_1 (mm)	L_2 (mm)	l (mm)	M	A (10^{-2} K mm^{-1})	B (10^{-4} K mm^{-2})	C (10^{-4} K mm^{-2})	ΔE_{geom}^{SED} (meV)	ΔE_{geom}^{DC} (meV)	Temperature control
6	2005	1805	200	0.900	0	0	0	43.8	—	Uniform temperature
					−1.648 (−1.655)	0	0	18.8	—	1D linear
					−1.648 (−1.655)	1.436 (1.452)	0	15.5	—	1D quadratic
					−1.648 (−1.655)	1.436 (1.452)	1.433 (1.452)	11.0 (10.8)†	—	2D quadratic
10	2019	1794	225	0.889	0	0	0	100.9	100.6	Uniform temperature
					−3.088 (−3.099)	0	0	24.4	21.5	1D linear
					−3.088 (−3.099)	1.804 (1.835)	0	21.3	15.2	1D quadratic
					−3.088 (−3.099)	1.804 (1.835)	1.814 (1.835)	16.9 (17.9)†	9.3 (5.2)‡	2D quadratic
25	2019	1794	225	0.889	0	0	0	288.1	295.2	Uniform temperature
					−7.723 (−7.749)	0	0	45.0	21.5	1D linear
					−7.723 (−7.749)	1.714 (1.835)	0	44.5	15.8	1D quadratic
					−7.723 (−7.749)	1.714 (1.835)	1.814 (1.835)	44.1 (44.7)†	9.3 (10.9)‡	2D quadratic

† The values in the parentheses are given by equation (9). ‡ The values in the parentheses are given by equation (10).

position of 5 µm × 5 µm (r.m.s.). We considered different gradient models including uniform temperature (no gradient), 1D linear, 1D quadratic and 2D quadratic (where the 1D gradients are always in the analyzer scattering plane), as given in Table 3. The temperature profile of the analyzer surface was determined by calculating several pixel temperatures and fitting to linear or quadratic equations. The parameters directly calculated from equation (7) are also listed in brackets and are generally close to the values estimated from the ray tracing. Each crystallite was assumed to have uniform temperature. To compare the experimental results, as presented in Section 6, a 2 mm × 2 mm SED was assumed in the case d = 6 mm, while a pixel size of 0.172 mm was used in the cases d = 10 and 25 mm to match the experimental conditions (PILATUS detector). The analyzer shape and size were taken as given in Table 1. The calculations were carried out assuming the incident bandwidth was a delta function which is then scanned (*i.e.* there is no convolution with the incident monochromator bandwidth).

4.1. d = 6 mm (single-element detector)

Fig. 5 shows how the TG improves the geometric term of energy resolution in the case d = 6 mm. The left-hand panels show the magnitude of aberration for rays onto the analyzer surface as a function of vertical position (y_a). To clarify the origin of this, four horizontal positions (x_a = 0, 20, 30 and 45 mm) are plotted. The right-hand panels show geometric energy resolution from all rays. Using uniform temperature, the energy resolution was obtained at ΔE_{geom} = 43.8 meV (FWHM, full width at half-maximum), as shown in Fig. 5(*a*). It is clear that the asymmetric line shape largely arises from the vertical analyzer extent and the horizontal geometric aberrations have only a small impact. Applying a linear TG correction, the energy resolution improved to ΔE_{geom} = 18.9 meV (FWHM) [Fig. 5(*b*)]. In addition, when applying a 1D quadratic TG, the energy resolution was slightly improved from the linear state as ΔE_{geom} = 15.5 meV (FWHM) and line shapes became more symmetric [Fig. 5(*c*)]. A 2D quadratic TG resulted in ΔE_{geom} = 11.1 meV (FWHM). The 2D quadratic TG yields the best resolution in the four cases, as shown in Fig. 5(*d*), and the geometric energy resolution for an SED is determined by the crystallite size.

4.2. d = 10 mm (dispersion compensation)

The calculation for d = 10 mm was performed in the same way as for d = 6 mm. The left-hand panels in Fig. 6 show the magnitude of aberration for selected x_a positions. The right-hand panels in Fig. 6 show the geometric resolution with an effective SED, *i.e.* integral over the spot defined by 11 × 11 pixels (∼1.9 mm × 1.9 mm). The energy resolution improved

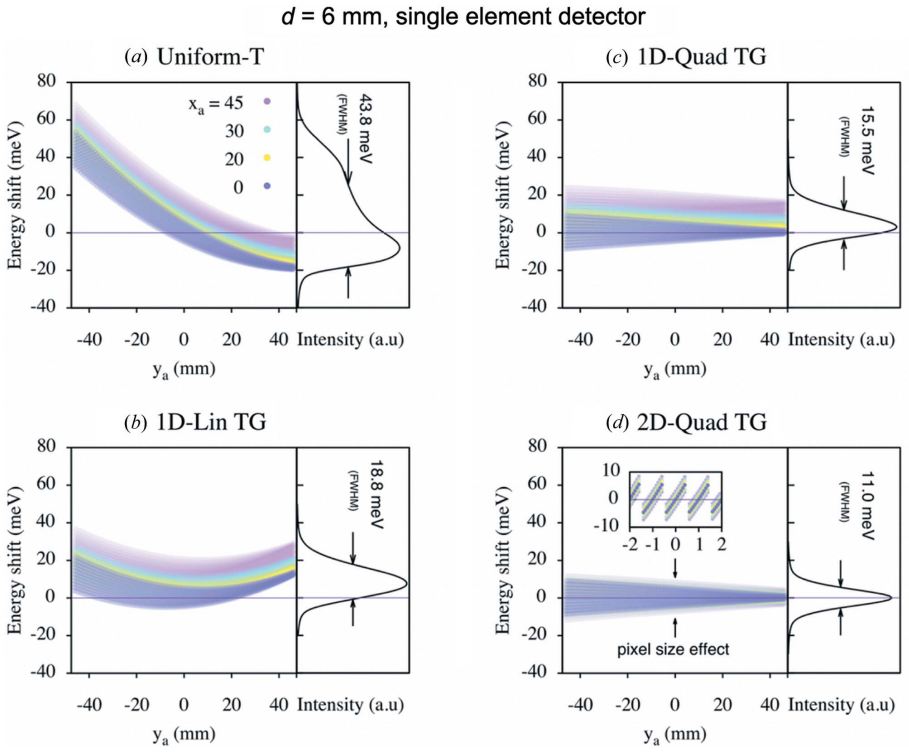

Figure 5
Calculation of the analyzer response for d = 6 mm. (*a*) Uniform temperature, (*b*) 1D linear TG, (*c*) 1D quadratic TG and (*d*) 2D quadratic TG. The left part of each figure shows the energy shift versus analyzer vertical position (y_a) with selected positions x_a = 0, 20, 30 and 45 mm while the right parts show the geometric contribution to the energy resolution for SEDs (2 mm × 2 mm).

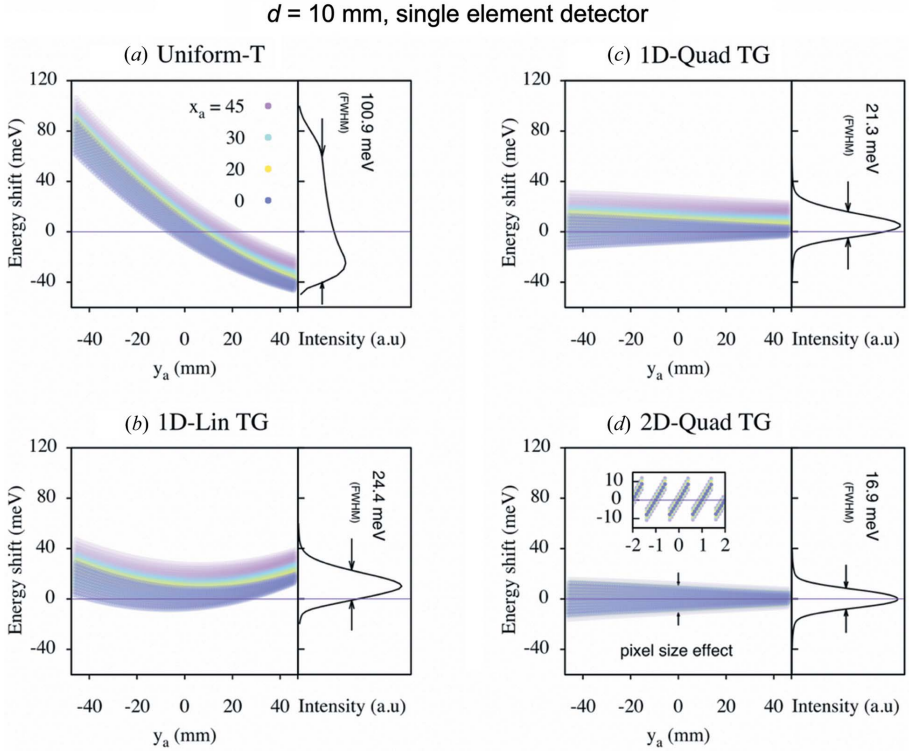

Figure 6
Calculation of the analyzer response for d = 10 mm. Same as Fig. 5 but with the effective SED defined by 11 × 11 pixels (~1.9 mm × 1.9 mm).

from ΔE_{geom} = 101 meV (FWHM) at uniform temperature to 17 meV (FWHM) at the 2D quadratic TG. The 'effective SED' resolution can be slightly improved by DC with a PSD. The left-hand panels in Fig. 7 show the geometric aberrations as a function of detector vertical position (y_d). Here, four selected horizontal positions (x_a = 0, 20, 30 and 45 mm) were plotted. The energy–position correlation at detector vertical position (y_d) is not completely linear in the off-Rowland geometry. However, the relation can be approximated as linear in the 2D TG. The right-hand panels in Fig. 7 represent geometric resolution in each detector pixel. The thick lines show DC-corrected results in each TG condition. The resolutions are summarized in Table 3. The DC correction does not work without a TG [Fig. 7(*a*)], but, by using both, the geometric resolution was much improved with ΔE_{geom} = 22, 15 and 9 meV (FWHM) for 1D linear, 1D quadratic and 2D quadratic TGs, respectively [Figs. 7(*b*)–7(*d*)].

4.3. d = 25 mm (dispersion compensation)

TG-dependent geometrical aberrations in the case d = 25 mm are shown in Fig. 8. Compared with d = 10 mm, the geometric energy resolutions have broader features in all the TG conditions. The energy resolution with an effective SED improved from ΔE_{geom} = 288 meV (FWHM) at uniform temperature to 45 meV (FWHM) at the 1D linear TG. However, no further improvements were obtained in the 1D and 2D quadratic TGs. The resolution with an SED can be improved by DC with a PSD. The energy–position correlation is not completely linear in the off-Rowland geometry. However, the relation can be approximated as linear in the 2D quadratic TG similar to d = 10 mm. The resolutions are summarized in Table 3. The DC correction does not work without a TG [Fig. 9(*a*)], but, by using both, the geometric contribution to the resolution was much improved with ΔE_{geom} = 22, 16 and 9 meV (FWHM) for 1D linear, 1D quadratic and 2D quadratic TGs,

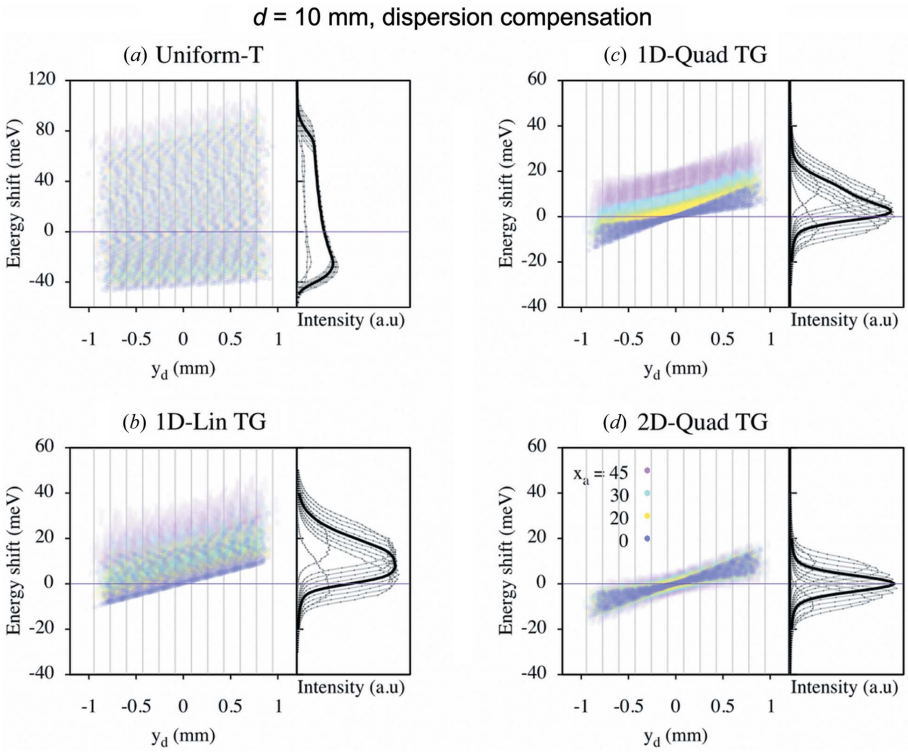

Figure 7
The relation of energy shift and detector vertical position (y_d) in the case d = 10 mm. Left-hand plots: energy–position correlation with selected analyzer positions x_a = 0, 20, 30 and 45 mm. The gray vertical lines correspond to a detector pixel size of 0.172 mm. Right-hand plots: geometric energy resolution obtained by ray-tracing calculations with DC. Slope error and source-size effect are included (see the main text). The thick lines are dispersion-corrected data.

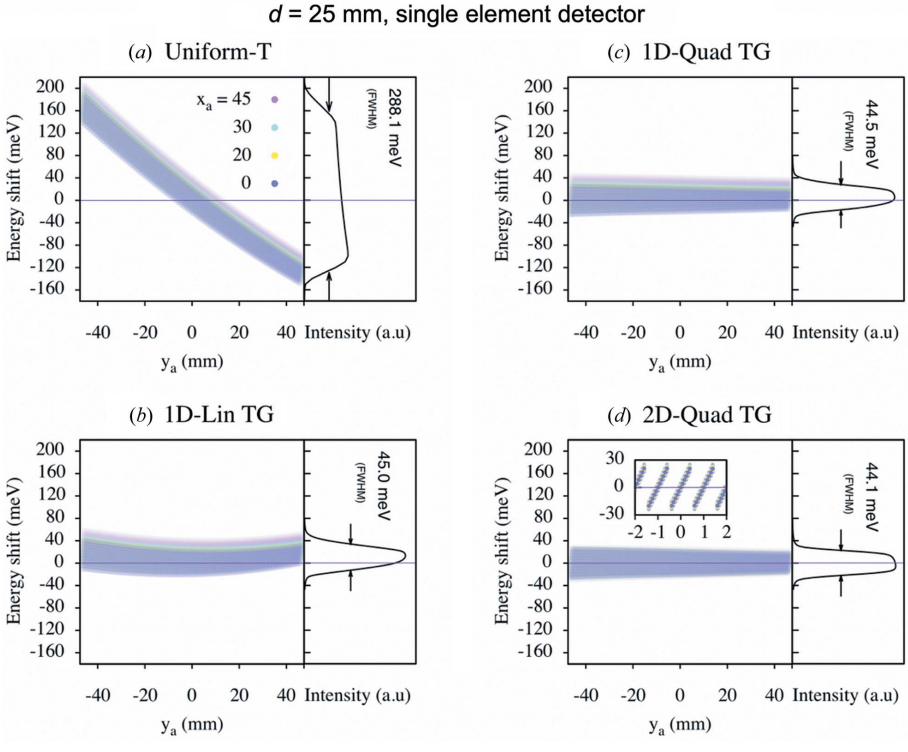

Figure 8
Calculation of the analyzer response for d = 25 mm. Same as Fig. 6.

respectively [Figs. 9(*b*)–9(*d*)]. The best estimated resolution 2D quadratic TGs in d = 10 and 25 mm are limited by the 0.172 mm pixel size of the detector.

5. Establishing and controlling the temperature gradient

We applied a 1D quadratic TG for the IXS analyzers. The basic concept is the thermal circuit of Ishikawa *et al.* (2015) with some improvements. The analyzer is placed between two separated brackets. The top and bottom of the substrate are polished flat to better than 0.02 mm with the surfaces parallel to 0.2 mrad. To increase thermal contact conductance, GaInSn eutectic was used. Two heaters were used: the main heater for the base temperature control and the other as an offset heater for controlling the TG. The arrows in Fig. 10 indicate the thermal flow of the system. Eight temperature sensors (two-wire readout, $\phi \simeq 2$ mm-diameter glass-encapsulated thermistors, OMEGA 55016) were attached on the side of the analyzer substrate. Feedback for the temperature control used a multi-channel switching digital multi-meter (Keithley 3706 and 3724) and a DC power supply (Wiener MPOD). Five temperature sensors ($T_1 \rightarrow T_5$, hot → cold, with a 20 mm pitch) are mounted on one side of the substrate and three temperature sensors ($T_6 \rightarrow T_8$, hot → cold, 40 mm pitch) were mounted on the other side [Figs. 11(*a*) and 11(*b*)]. Here, T_3 and T_7 were placed in the middle of the analyzer in the main TG direction. The feedback parameters for the base temperature and the offset temperature were $T_0 = (T_3 + T_7)/2$ and $\Delta T_g = 0.5[T_1 + T_6 - (T_5 + T_8)]$ K per 80 mm, respectively. The magnitude of the gradient used here is much larger than the ∼0.01°C per 100 mm used with high-resolution analyzers (Ishikawa *et al.*, 2015). In addition, the non-linear TG must be taken into account. The non-linear TG is not simple but it is possible by changing the thermal flow of the system. One way is to add a triangular prism object onto the backside of the analyzer substrate, as seen in Fig. 12(*a*) where a finite-element analysis using *ANSYS* is shown. Practically, owing to

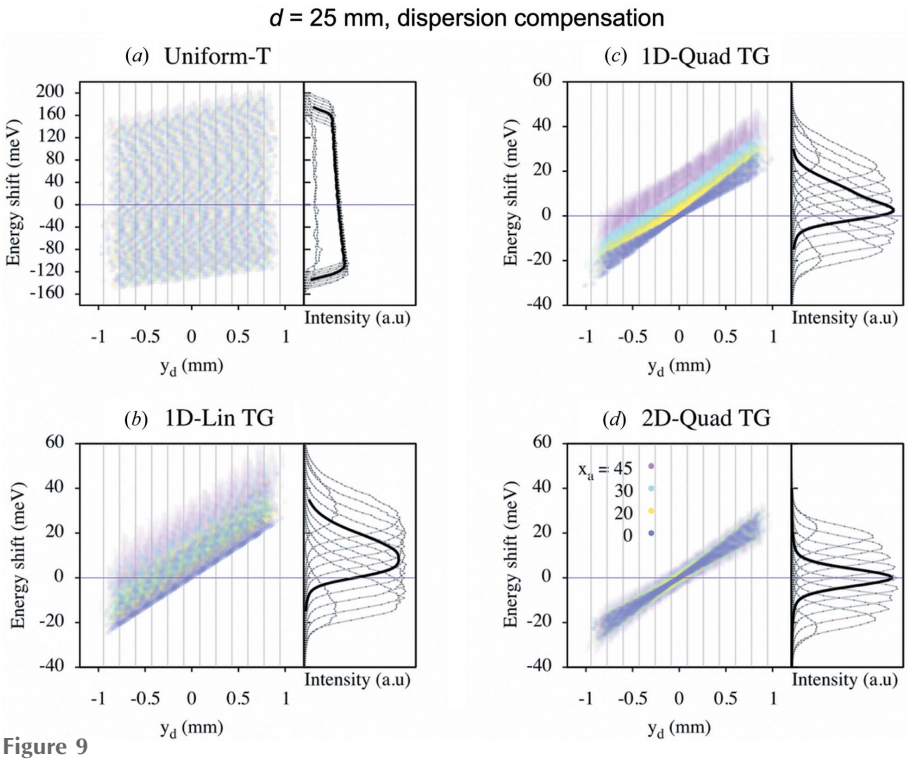

Figure 9
Relation of energy shift and detector vertical position (y_d) in the case d = 25 mm. Same as Fig. 7.

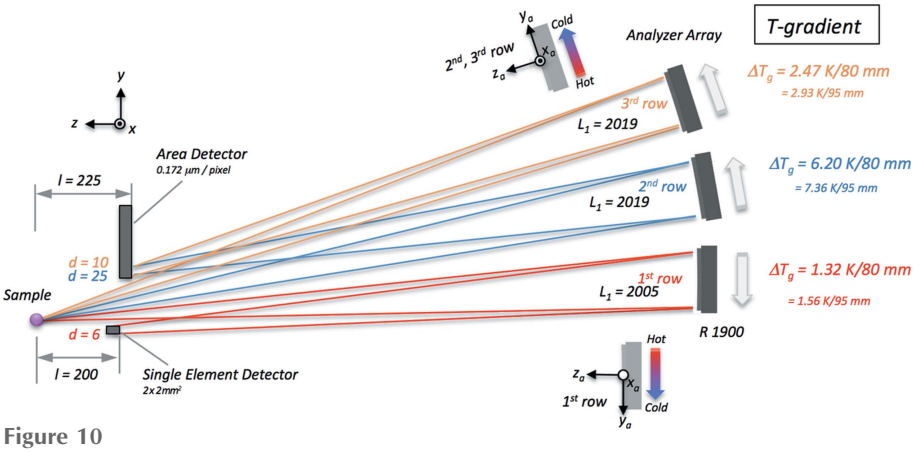

Figure 10
A schematic of the focusing geometry of the multi-analyzer array installed at the medium-resolution spectrometer of BL43LXU at SPring-8 (view from the side). The detectors are placed 200 and 225 mm away from the sample to make space for sample environments. The focusing geometry is an off-Rowland geometry: the focal point is on the detectors. The first-row analyzers focus onto 2 mm × 2 mm CdZnTe SEDs. The second and third rows of analyzers focus onto the lower edge of the area detector (DECTRIS, PILATUS 100K, 0.172 mm pixel^{-1}). Furthermore, l refers to the horizontal distances between the sample and the detectors, and d is the vertical offset between the center of the scattered rays and the center of the focal spot. The magnitude of the TG depends on each of the geometric conditions. The arrows indicate thermal flow direction (hot → cold).

the complexity of the thermal contact conductance depending on surface roughness, contact pressure and interface material, the material of the non-linear TG object was determined by experiment. The geometry for the 2D TG is presented in Fig. 12(*b*) where the additional heater and jig may be seen.

In the case d = 6 mm, SK3 (a carbon-steel defined Japan Industrial Standard), with a thermal conductivity of 35 W m^{-1} K^{-1}, was used to control thermal flow for creating a 1D quadratic temperature curve. Note that in the y_a direction there is more than a factor of two difference in T: $\Delta T(y_a = -40\ \text{mm}) = 1.11°\text{C}$, while $\Delta T(y_a = +40\ \text{mm}) = -0.46°\text{C}$. The ideal analyzer temperature is given by equation (7) as $A = -1.648 \times 10^{-2}$ K mm^{-1}, $B = 1.433 \times 10^{-4}$ K mm^{-2} and $C = 0$ K mm^{-2}. The elastic temperature and magnitude of TG were set at $T_0 = 27°\text{C}$ and ΔT_g = 1.32 K per 80 mm, respectively. The feedback parameters for the base heater and the offset heater were T_0 and ΔT_g, respectively. The typical applied power for the offset heater was ∼0.8 W, while the chiller temperature was set at 25°C. Fig. 11(*c*) (left) shows the temperature of each sensor as a function of analyzer position. The magnitude of the desired TG is 1.32 K per 80 mm. The measured temperatures using the 1D quadratic TG agree well with the ideal curve. In the cases d = 10 and 25 mm, the magnitudes of ithe ideal ΔT_g are 2.47 K per 80 mm and 6.2 K per 80 mm, respectively. The materials of the attachment jig for creating the 1D quadratic TG are given in Table 4. Despite a large temperature offset, substrate temperature can be controlled well for more than a month, as shown in Fig. 11(*c*) (right).

6. Results and discussion

Tests were performed at the medium-resolution spectrometer of BL43LXU (Baron, 2010; Ishikawa *et al.*, 2017) at the RIKEN SPring-8 Center in Japan. The bandwidth of the X-rays from the undulator was reduced first by a liquid-nitrogen-cooled high-heat-load mirror, then a high-heat-load Si(111) monochromator followed by a nested-channel-cut medium-resolution monochromator consisting of Si(440) and Si(660) crystals. The focal-spot size at the sample was 25 μm (V) × 30 μm (H) (FWHM) after focusing by an elliptically bent cylindrical mirror. The total energy resolution of the spectrometer was measured using a 2 mm-thick polymethylmethacrylate sample with the analyzer placed at the structure-factor maximum. The full analyzer surface was illuminated, corresponding to momentum resolution of $\Delta Q \simeq 3.6$ nm^{-1} (full width) at 15.816 keV. The incident energy was scanned by changing both channel-cut crystal angles, while the analyzer temperatures and angle were kept constant. The analyzers

Table 4
Experimental energy resolution using a 1D quadratic TG.

λ: thermal conductivity (representative value). A, B: temperature coefficients as a function of analyzer position, as explained in the main text. $\Delta E_{\rm tot}^{\rm SED}$: the experimental total energy resolution (FWHM) using an SED [2 mm × 2 mm for d = 6 mm, and ∼1.9 mm × 1.9 mm (11 × 11 pixels) for d = 10 and 25 mm]. $\Delta E_{\rm tot}^{\rm DC}$: the experimental total energy resolution (FWHM) for DC correction [∼1.9 mm × 0.172 mm (11 × 1 pixels)].

								Calculations (geometric)		Experiment (total)	
d (mm)	Attachment material	λ (W m^{-1} K^{-1})	A (10^{-2} K mm^{-1})	B (10^{-4} K mm^{-2})	$\Delta T_{\rm g}$ (K per 80 mm)	$\Delta E_{\rm int}$ (meV)	$\Delta E_{\rm inc}$ (meV)	$\Delta E_{\rm geom}^{\rm SED}$ (meV)	$\Delta E_{\rm geom}^{\rm DC}$ (meV)	$\Delta E_{\rm tot}^{\rm SED}$ (meV)	$\Delta E_{\rm tot}^{\rm DC}$ (meV)
6	SK3	34.7	−1.6476	1.4355	1.32	4.4	22	15.5	–	25.0	–
10	SUS440C	24.3	−3.0880	1.8036	2.47	4.4	22	21	15	31.7	25.4
25	SUS304	16.3	−7.7229	1.7140	6.20	4.4	22	45	16	57.0	32.4

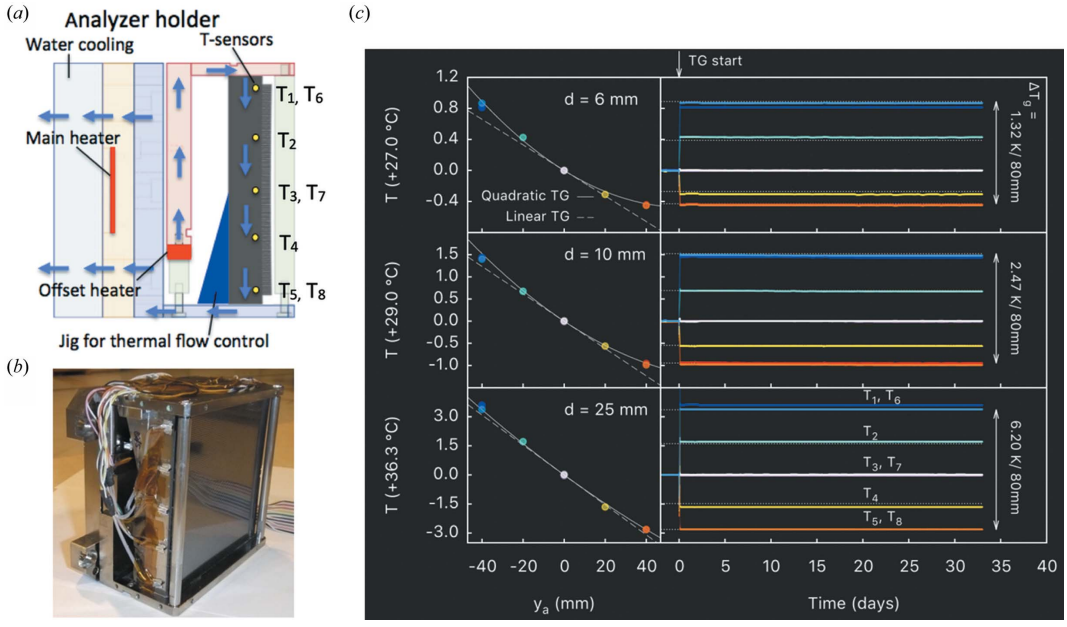

Figure 11
(*a*) A schematic of the analyzer holder used to apply a non-linear (1D quadratic) TG (view from the side). The arrows indicate thermal flow. Temperature sensors (T_1–T_8) were attached onto the side of the analyzer substrate. (*b*) Photograph of the analyzer holder. (*c*) Measured 1D quadratic TGs (left) and their long time stability (right) after TG creation.

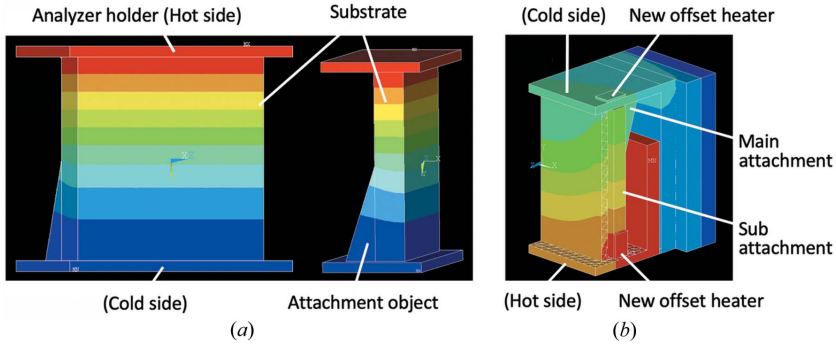

Figure 12
Finite-element analysis for non-linear TGs using *ANSYS*. (*a*) 1D quadratic TG. A triangular prism is attached onto the backside of the analyzer substrate. This creates a non-linear TG on the surface. (*b*) One possible design that might be used to create a 2D quadratic TG with additional jig and heaters on the side of the analyzer substrate. Half of the analyzer is shown.

were mounted inside a vacuum chamber on the 2θ arm. The energy scale was calibrated using a diamond phonon at 164.7 meV as described by Fukui *et al.* (2008). Three different analyzer geometries in the cases d = 6, 10 and 25 mm were tested.

The TG is effective when used with DC and is particularly advantageous for a multi-analyzer array that requires large deviations from the exact Rowland circle condition. In the present spectrometer, X-rays from second and third rows were detected by a PSD using DECTRIS PILATUS 100K-SP8

(0.172 mm pixel^{-1}), as shown in Fig. 10. The detector was specially fabricated to allow operation in vacuum with nearly no border on one side allowing a relatively tight clearance between the beam and the detector. The analyzer focus was near the edge of the active element in the vertical direction (y_a) to keep the Bragg angle as close as possible to backscattering (smaller δ_0); while the horizontal axis (x_a) was the same as the sample–analyzer axis. Note that the TG direction (arrows in Fig. 10) inverts depending on downward or upward reflection.

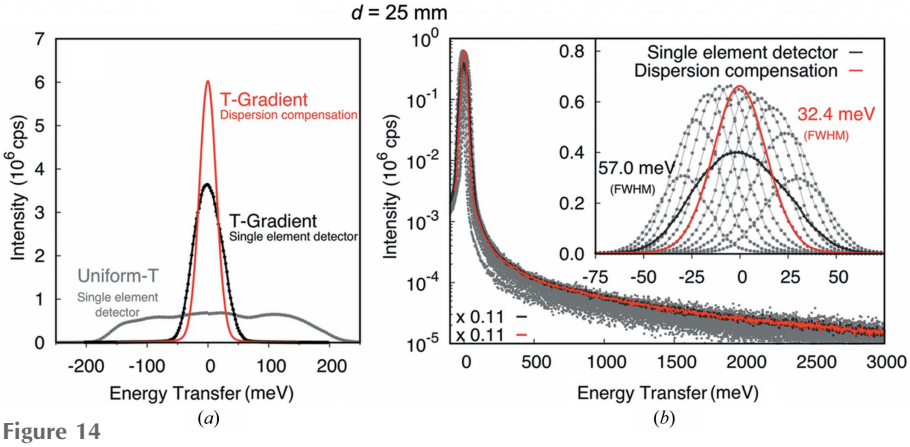

Figure 14
Measured energy resolution in the case d = 25 mm. (*a*) The comparison between uniform temperature and the 1D quadratic TG (ΔT_g = 6.2 K per 80 mm) with an effective SED (11 × 11 pixels) and DC correction (11 × 1 pixels). The integrated intensity is conserved in both uniform temperature and TG. (*b*) Energy resolution with 1D quadratic TG. Gray, the resolution from each pixel (11 × 1 pixels); black, effective SED; and red, DC-corrected signals. The intensities of the effective SED and DC are scaled (×0.11).

6.1. Results at d = 6 mm (single-element detector)

The first (bottom) row of analyzers (see Table 2 and Fig. 10) focused X-rays onto three CdZnTe SEDs of 2 mm × 2 mm. The experimental energy resolution was measured to be 60 meV (FWHM, 49 mrad × 46 mrad) with uniform temperature. The line shape was asymmetric similar to the simulation results in Fig. 5(*a*). To improve total energy resolution, a 1D quadratic TG was applied as explained in Section 5. The total energy resolution improved from 60 to 25 meV (FWHM) after the TG application (Fig. 13). Not only the line width but also the line shape improved. Investigation of *d*–*d* excitations in NiO (Ishikawa *et al.*, 2017) revealed both lattice and magnetic effects using this 25 meV resolution. For Bragg angles close to backscattering, δ_0 < ∼2 mrad, an SED provides good resolution using only an appropriate TG. However, when further from backscattering, δ_0 > ∼2 mrad, only a TG was not sufficient, so DC was applied. This is particularly important for multi-analyzer geometries as explained in Section 6.2.

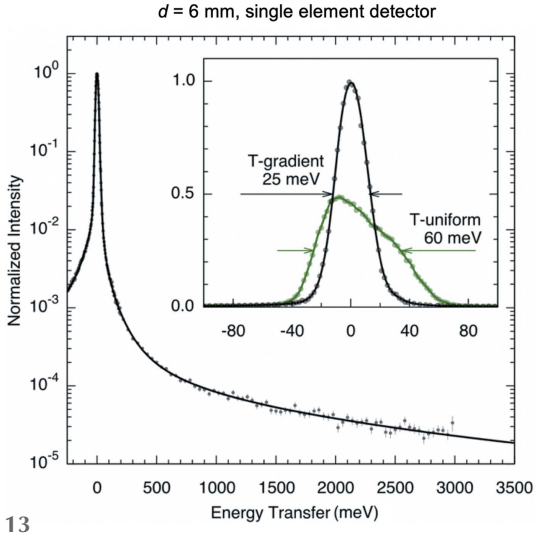

Figure 13
Measured energy resolution at d = 6 mm (first-row analyzer) and 1D quadratic TG (ΔT_g = 1.32 K per 80 mm), observed by an SED (2 mm × 2 mm). The inset shows the uniform-temperature case for comparison.

6.2. Results at d = 25 mm (dispersion compensation)

The second analyzer row focused the beam onto the area detector with d = 25 mm (Table 2). Of the three analyzer rows, the second-row analyzer has the largest deviation from backscattering so requires the largest TG, ∼7 K per 95 mm. The total energy resolution with uniform temperature results in ΔE_{tot} = 330 meV for an effective SED (11 × 11 pixels) and DC (11 × 1 pixels), as shown in Fig. 14(*a*). The observed focal-spot image at elastic energy is shown in Fig. 15(*a*) and is comparable with the ray-tracing results shown in Fig. 15(*c*). Thus, it is clear that DC does not improve energy resolution without a TG. We applied a 1D quadratic TG for this geometry. The required TG is ΔT_g = 6.2 K per 80 mm, as listed in Table 4. A SUS304 jig[1] was used for the 1D quadratic TG (Table 4). To align elastic energy with first-row analyzers, the central analyzer temperature T_0 was set to 36.3°C, as is needed to put the elastic peak at the same energy as the first-row analyzers. With the additional jig, the feedback parameters T_0 = 36.3°C and ΔT_g = 6.2 K per 80 mm create close to the desired 1D quadratic TG given in equation (7), where A and B are listed in Table 4. The required power to apply the TG was ∼5.7 W for the offset heater, when cooling water temperature was kept at 32.5°C. Fig. 11(*c*) shows temperature stability – each temperature was stable for more than a month. Applying the 1D quadratic TG, the focal-spot image on the detector became narrower [Fig. 15(*b*)] owing to the correction of chromatic aberration. The line shape of the resolution also drastically narrowed [Fig. 14(*a*)]. It is worth noting that the integrated intensity is conserved before and after the TG.

[1] Practically, the jig has a slightly larger quadratic coefficient than predicted, so a thin layer of Kapton is added between the jig and the analyzer to reduce thermal contact conductance.

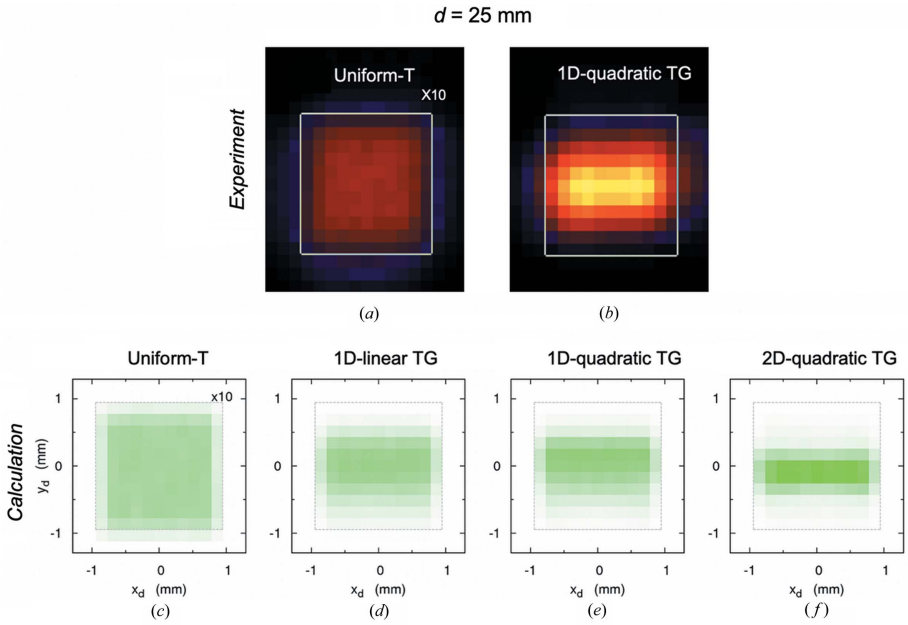

Figure 15
Focal-spot images at the elastic energy from second-row analyzer (d = 25 mm). (a), (b) Experiment. (c)–(f) Ray-tracing calculations. White squares in (a) and (b) and broken lines in (c)–(f) indicate the border of the effective SED defined by 11 × 11 pixels (∼1.9 mm × 1.9 mm), which is slightly larger than the estimated focal-spot size [$c(1 + M)$ = 0.87 × 1.89 = 1.65 mm]. The full analyzer acceptance (49 mrad × 46 mrad) is irradiated. For clarification, the color scales of (a) and (c) are enhanced by a factor of ten more than the others. For calculation, a slope error of 20 µrad × 20 µrad (r.m.s.) and a source size of 5 µm × 5 µm (r.m.s.) were assumed. The incident bandwidth and intrinsic reflection width are not included.

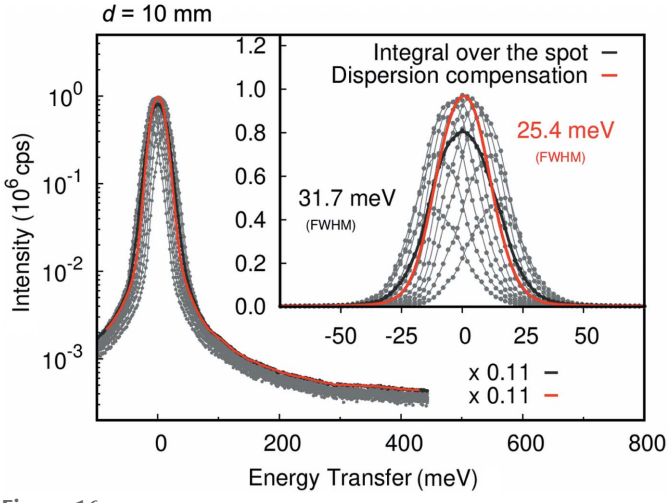

Figure 16
Measured energy resolution in the case d = 10 mm with 1D quadratic TG (ΔT_g = 2.47 K per 80 mm). The intensities of the effective SED and DC are scaled (×0.11).

The energy resolution with the TG was found to be ΔE_{tot} = 57.0 meV (FWHM) with an effective SED [Fig. 14(b)]. The energy resolution of each pixel improved to 30–38 meV (FWHM). As a consequence, the energy resolution with DC[2] yields ΔE_{tot} = 32.4 meV (FWHM) [Fig. 14(b)]. The discrepancy from calculation may be largely from imperfect temperature correction away from the center of the analyzer. We obtained ΔE_{tot} = 23.7 meV (FWHM) resolution when the analyzer acceptance was reduced by a factor of three in each direction.

6.3. Results at d = 10 mm (dispersion compensation)

The third analyzer row was also designed to focus onto the area detector as shown in Fig. 10. The experimental total energy resolution at uniform temperature was obtained at ΔE_{tot} = 100 meV (FWHM) with an effective SED or with DC. The results agree well with the calculated ΔE_{geom} = 101 meV (FWHM). Similar to the d = 25 mm case of Section 6.2, DC does not improve energy resolution without a TG. To apply a non-linear TG, pieces of stainless steel (SUS440C, λ = 24 W m^{-1} K^{-1}) were attached to the backside of the Invar substrates [see Fig. 11(a)]. To align elastic energy with first-row analyzers, T_0 was set to ∼29.0°C. The feedback parameters T_0 = 29.0°C and ΔT_g = 2.47 K per 80 mm enabled the 1D quadratic TG that is listed in Table 4. The practical power for the TG was typically ∼1.6 W for the offset heater, when the temperatures of the base and the cooling water were 29°C and 25°C, respectively. By applying the 1D quadratic TG, the energy resolution improved to ΔE_{tot} = 31.7 meV (FWHM) using an effective SED (11 × 11 pixels), as shown in Fig. 16. Using DC, the energy resolution improved to 25–27 meV (FWHM) depending on the detector pixel positions. Consequently, the final corrected resolution[3] ΔE_{tot} = 25.4 meV (FWHM) was obtained.

7. Conclusions

We have shown that careful application of temperature gradients on diced spherical analyzers in a Si(888) backscattering geometry allowed us to improve the energy resolution between two and ten times without loss of signal intensity. The temperature gradient allows relaxing of the Rowland geometry (magnification of 0.9) and allows a large space for the sample, making more complicated sample environments possible. We obtained a factor of 2.4 improvement in resolution, with a best case of 25 meV resolution (FWHM, 49 mrad × 46 mrad acceptance) with a single-element detector. A combination of DC correction and a temperature gradient improved the energy resolution by a

[2] Strictly, the energy–position correlation is not completely linear in the off-Rowland geometry (Ishikawa & Baron, 2010). However, a linear energy–position correlation is almost valid in these geometries. Position-sensitive data were shifted (y_d direction) by 5.6 meV pixel^{-1} (d = 25 mm) and summed.

[3] Position-sensitive data were shifted (y_d direction) by 2.6 meV pixel^{-1} (d = 10 mm) and summed.

factor of ten, with a best case of 32 meV FWHM. In both cases, the measured resolution includes the incident-beam contribution of $\Delta E_{\rm inc}$ = 22 meV. Note that further improvement of the overall energy resolution would be possible if the incident bandwidth and/or detector pixel size were reduced. We expect a similar temperature-gradient approach may improve in hard X-ray high-resolution RIXS (ΔE < ~30 meV) with spherical analyzers.

Acknowledgements

The authors acknowledge K. Miura, Y. Senba and H. Ohashi for evaluating the surface profile of wafers and substrates. DI thanks S. Takahashi and Y. Senba for help with the finite-element tools.

References

Baron, A. Q. R. (2010). *SPring-8 Inf. Newsl.* **15**, 14–19.
Baron, A. Q. R. (2016). *Synchrotron Light Sources and Free-Electron Lasers: Accelerator Physics, Instrumentation and Science Applications*, edited by E. Jaeschke, S. Khan, J. R. Scheider & J. B. Hastings, pp. 1643–1757. Cham: Springer International Publishing.
Baron, A. Q. R. (2020). *arXiv*:1504.01098.
Baron, A. Q. R., Tanaka, Y., Goto, S., Takeshita, K., Matsushita, T. & Ishikawa, T. (2000). *J. Phys. Chem. Solids*, **61**, 461–465.
Burkel, E. (1991). *Inelastic Scattering of X-rays with Very High Energy Resolution*. Springer-Verlag Berlin Heidelberg.
Fukui, H., Katsura, T., Kuribayashi, T., Matsuzaki, T., Yoneda, A., Ito, E., Kudoh, Y., Tsutsui, S. & Baron, A. Q. R. (2008). *J. Synchrotron Rad.* **15**, 618–623.
Haverkort, M. W., Tanaka, A., Tjeng, L. H. & Sawatzky, G. A. (2007). *Phys. Rev. Lett.* **99**, 1–4.
Huotari, S., Albergamo, F., Vankó, G., Verbeni, R. & Monaco, G. (2006). *Rev. Sci. Instrum.* **77**, 053102.
Ishikawa, D. & Baron, A. Q. R. (2010). *J. Synchrotron Rad.* **17**, 12–24.
Ishikawa, D., Ellis, D. S., Uchiyama, H. & Baron, A. Q. R. (2015). *J. Synchrotron Rad.* **22**, 3–9.
Ishikawa, D., Haverkort, M. W. & Baron, A. Q. R. (2017). *J. Phys. Soc. Jpn*, **86**, 093706.
Larson, B. C., Ku, W., Tischler, J. Z., Lee, C. C., Restrepo, O. D., Eguiluz, A. G., Zschack, P. & Finkelstein, K. D. (2007). *Phys. Rev. Lett.* **99**, 2–5.
Masciovecchio, C., Bergmann, U., Krisch, M., Ruocco, G., Sette, F. & Verbeni, R. (1996). *Nucl. Instrum. Methods Phys. Res. B*, **117**, 339–340.
Mohr, P. J., Newell, D. B. & Taylor, B. N. (2016). *Rev. Mod. Phys.* **88**, 035009
Okada, Y. & Tokumaru, Y. (1984). *J. Appl. Phys.* **56**, 314–320.
Said, A. H., Sinn, H. & Divan, R. (2011). *J. Synchrotron Rad.* **18**, 492–496.
Schülke, W. (2007). *Electron Dynamics by Inelastic X-ray Scattering*. Oxford University Press.
Sinn, H. (2001). *J. Phys. Condens. Matter*, **13**, 7525–7537.
Sinn, H., Moldovan, N. A., Said, A. H. & Alp, E. E. (2002). *Proc. SPIE*, **4783**, 123.
Verbeni, R., Kocsis, M., Huotari, S., Krisch, M., Monaco, G., Sette, F. & Vanko, G. (2005). *J. Phys. Chem. Solids*, **66**, 2299–2305.
Verbeni, R., Pylkkänen, T., Huotari, S., Simonelli, L., Vankó, G., Martel, K., Henriquet, C. & Monaco, G. (2009). *J. Synchrotron Rad.* **16**, 469–476.
Watanabe, H., Yamada, N. & Okaji, M. (2004). *Int. J. Thermophys.* **25**, 221–236.